PCCP

Accepted Manuscript

ROYAL SOCIETY OF CHEMISTRY

www.rsc.org/pccp

Applications of ALD MnO to Electrochemical Water Splitting

Katie L. Pickrahn,[a,§] Yelena Gorlin,[a,§,c] Linsey C. Seitz,[a] Aaron Garg,[a]
Dennis Nordlund,[b] Thomas F. Jaramillo,[a] and Stacey F. Bent [a,*]
[a] Department of Chemical Engineering, Stanford University,
Stanford, CA 94305-5025, USA
[b] SLAC National Accelerator Laboratory, 2575 Sand Hill Rd,
Menlo Park, California 94025, United States
[c] Department of Chemistry, Technische Universität München,
Arcisstraße 21, 80333 München, Germany
*sbent@stanford.edu
[§]These authors contributed equally to this work.

Atomic layer deposition (ALD) is an attractive method to deposit uniform catalytic films onto high surface area electrodes. One interesting material for ALD synthesis is MnO_x, a promising earth-abundant catalyst for the oxygen evolution reaction (OER). It has previously been shown that catalysts beginning as MnO synthesized using ALD on smooth glassy carbon (s-GC) electrodes and the Mn_2O_3 obtained upon annealing the MnO s-GC are active OER catalysts. Here, we use ALD to deposit MnO on high surface area GC (HSA-GC) substrates, forming an active catalyst on a geometric surface area basis. We then characterize three types of catalysts, HSA-GC MnO, s-GC MnO, and annealed MnO (Mn_2O_3), using cyclic voltammetry (CV), scanning electron microscopy (SEM), and *ex-situ* X-ray absorption spectroscopy (XAS). We show that under OER conditions, all three catalysts oxidize to similar surface states with a mixture of Mn^{3+}/Mn^{4+} and that MnO_x surface area effects can account for the observed differences in the catalytic activity. We also demonstrate the need for a high surface area support for high OER activity on a geometric basis.

I. Introduction:

ALD is a promising deposition technique for the fabrication of catalysts for both fundamental studies and devices.[1-5] The technique consists of a series of self-limiting, saturated reactions that deposit up to one monolayer of material at a time.[6-8] Often used in the semiconductor industry, the main advantage of this synthesis method is its capability to fabricate high quality, conformal films with fine control over the film thickness. Such fine deposition control makes ALD an attractive technique for catalysis, particularly catalysts for the photoelectrochemical (PEC) generation of solar fuels,[9, 10]

where nanostructuring is proving to be an effective strategy to improve the efficiency of devices.[2, 11-15]

In the PEC generation of solar fuels, a process in which solar energy is stored in the form of chemical bonds, catalysts are essential to efficiently driving the thermodynamically uphill chemical reactions.[10, 16] The oxygen evolution reaction (OER), a reaction involving the transfer of four electrons, is particularly difficult to catalyze and often associated with sluggish kinetics.[17] In an effort to accelerate development of PEC devices and other renewable energy technologies that rely on efficient OER catalysis, much research has focused on finding earth abundant catalysts based on first row transition metal oxides, including those of Co, Fe, Ni, and Mn, some of which have shown activity comparable to, if not better than, precious metal oxides in alkaline conditions.[18, 19] Although MnO_x does not have the highest activity of these materials, it has gained much attention as an OER catalyst due to its abundance, low toxicity, and low cost, and to Nature's use of MnO_x as the catalyst in the oxygen evolving center in photosystem II.[20-25] The activity of MnO_x varies according to preparation and different testing conditions, and correlation of the initial phase with activity is complicated by changes in structure and oxidation under OER-testing conditions.

Materials need to fulfill many requirements to serve as a good OER catalyst. For example, the electronic properties of a material must allow for efficient catalysis of the reaction, with surface-adsorbate interactions governing the quality of a catalyst.[26] The oxidation state of a material can impact these interactions, and a careful understanding of

the oxidation state is necessary to optimize the catalyst.[27, 28] Surface area is another important consideration for the geometric activity of a catalyst. The surface area may change with testing, and hydration can impact the number of electrochemically accessible sites. For electrocatalysts, another important design criteria is the ability of a charge to reach the active site with minimal overpotential due to ohmic loss. The use of nanoparticles or thin films can mitigate these effects in semiconducting electrocatalysts. ALD is an excellent method to deposit catalysts to meet these criteria. For example, a high population of active sites can be achieved by using ALD to deposit a conformal coating on a nanostructured substrate.[29] ALD can also achieve ultra-thin films of catalytic material, an architecture which can mitigate the ohmic losses in semiconducting catalysts.[30]

Another particularly promising use of ALD for PEC applications is the deposition of conformal, stabilizing coatings on a nanostructured light absorber. While it is often difficult to find a single material that meets all the demands of a PEC device, a nanostructured device architecture consisting of a stabilizing film on top of a light absorber of choice offers a way to separate the electrical and optical requirements of the semiconductor from the requirements for long-term stability.[31] The conformality and continuity of the film will protect the underlying light absorber by preventing access of the electrolyte to its surface, while the control over the thickness of the layer will help ensure that charge transport limitations and light absorption are minimized.[32, 33] These concepts have already been applied to PEC through demonstration of ALD-TiO_2 protective layers to stabilize Si, GaP, and GaAs photoanodes and Cu_2O photocathodes. [11,

[12, 34] In those studies, ALD allowed for the formation of a continuous thin film at small enough film thicknesses not achievable by other deposition methods.

To further reduce ohmic losses and parasitic light absorption, it may be advantageous to combine the catalyst and stabilizing roles into one material. The possible use of MnO_x as a simultaneous catalytic and protective layer in PEC devices has already been explored by Strandwitz and co-workers, who utilized ALD to deposit MnO on silicon photoanodes.[35] In that work, Strandwitz et al. found that the protective properties of MnO_x are only temporary and hypothesized that this was related to the changing oxidation state of the MnO_x under operating conditions. A deeper understanding of the phase changes in the catalyst is necessary for the proper optimization of the ALD-MnO catalyst for PEC applications.

In our previous work, which focused on the catalytic properties of ALD-MnO, we showed that MnO_x deposited with a starting phase of MnO by ALD on smooth glassy carbon (s-GC) is active for OER and that annealing MnO to form an initial phase of Mn_2O_3 results in a slight increase in activity.[36] Herein, we take a closer look at the properties of the catalysts under OER conditions. We characterize the catalysts using scanning electron microscopy (SEM) and X-ray absorption spectroscopy (XAS), and we show that the exposure of the surfaces to the OER conditions leads to a disruption in the conformal coating of the ALD film and results in oxidation of the Mn in all of the considered catalysts. The extent of the oxidation is dependent on the catalyst preparation. It appears that surface area is the main determinant of activity between the annealed and

as-deposited MnO_x thin films. We use ALD and a nanostructured substrate to synthesize an even more active MnO catalyst, confirming that annealing is not necessary to achieve high OER activity. We show that a nanostructured substrate is important and the same volume of MnO_x does not exhibit as high of an activity despite the large disruption in the conformal coating under OER conditions. The implications of these findings to the electrocatalyst design and to the fabrication of successful PEC devices are discussed.

II. Methods

MnO_x was deposited on the substrates using ALD, as described previously.[36, 37] Bis(ethylcyclopentadienyl) manganese ($Mn(CpEt)_2$, Strem) and water were used as the reactant and counter-reactant, respectively. The substrate was maintained at 175 °C and the $Mn(CpEt)_2$ bubbler was kept between 72-82 °C. The reaction consisted of a 2 second dose of either $Mn(CpEt)_2$ or H_2O followed by a purge of at least 50 seconds. Under these conditions, a growth rate ~ 1 Å/cycle was achieved. Samples were initially exposed to the atmosphere at ~ 175 °C.

Three types of MnO_x-GC catalysts were synthesized by ALD, as shown in **Table 1**. For s-GC MnO_x samples, polished glassy carbon substrates (HTW Hochtemperatur-Werkstoffe GmbH, SigradurG disks) were cleaned by sonication in water for 30 minutes and blown dry. ALD was then performed on the substrates, adjusting the number of cycles to achieve the appropriate thickness. To make annealed samples, s-GC MnO_x samples were annealed at 480 °C with a 3 hour ramp up time from room temperature. To make the HSA-GC supports, MnO_x was first electrodeposited onto the s-GC and then

annealed, following the same synthesis procedure described by Gorlin et al.[23] To remove the MnO_x after the sample was prepared, MnO_x coated substrates were immersed in 4 ml of 10 wt% hydrochloric acid solution overnight, then rinsed with Millipore water. This process was carried out because the presence of the MnO_x catalyzes the etching of the GC and leads to a more porous substrate similar to that observed in the annealed MnO_x ALD system. The resultant substrate had a porous morphology, as seen by SEM (Fig S1b). MnO_x was then deposited on the respective substrate by ALD, as described above.

Table 1:Types of catalysts explored in this study

Catalyst	**Substrate**	**MnO_x Coating**	**MnO_x Oxidation State (initial)**
s-GC MnO_x	Smooth GC	Conformal	MnO (surface oxidized)
HSA-GC MnO_x	HSA GC	Conformal	MnO (surface oxidized)
Annealed MnO_x	HSA GC	Partial	Mn_2O_3

The electrocatalytic properties of the samples were investigated by cyclic voltammetry (CV). Catalysts were mounted in a Teflon holder and loaded into a rotating disk electrode (RDE), 3-electrode set-up. A Ag/AgCl (sat'd KCl) electrode and a carbon rod served as the reference electrode and counter electrode, respectively, and samples were tested in 0.1 M KOH. A scan rate of 20 mV/s was used and measurements were *iR*-compensated at 85%. Samples were first cycled between 0.05 V_{RHE} and 1.1 V_{RHE} in N_2 saturated electrolyte to compare redox features. The electrolyte was then saturated with O_2, and scanned once again between the same potentials to measure the catalytic activity for oxygen reduction reaction, which is relevant for bifunctional catalysts. MnO_x

electrodes were then cycled between 0.05 V_{RHE} and 1.8 V_{RHE} in O_2 saturated electrolyte and in N_2 saturated electrolyte to characterize the OER. To prepare samples representative of extended exposure to OER conditions, after the above testing samples were held at 1.65 V_{RHE} for 30 minutes. All potentials were adjusted for reference to a reversible hydrogen electrode found by a calibration involving HER between two Pt electrodes.[23]

The MnO_x films were examined both before and after electrochemical testing. Film thickness was determined using ellipsometry (Woolam α-SE) on Si witness wafers present in the chamber during the deposition. Film morphology was characterized using an FEI Magellan 400XHR scanning electron microscope. *Ex*-situ XAS was used to analyze the oxidation state of the Mn by examining the Mn L-edge, as described previously.[38, 39] In short, samples were mounted on an aluminum bar and placed under ultra-high vacuum. Samples were measured on the 31-pole wiggler beamline 10-1 at the Stanford Synchrotron Radiation Lightsource (SSRL). Data was collected in both total electron yield (TEY) and Auger electron yield (AEY) mode. The XAS energy scale was adjusted to account for drift in the beam energy, and then shifted to a standard value, and the spectra were normalized as described elsewhere.[38] Powder MnO_x samples, spread out on conductive carbon tape, were used as MnO_x standards. Mn_3O_4 and Mn_2O_3 powders were purchased from Sigma-Aldrich and used as received. α-MnO_2 and γ-MnOOH were synthesized in the laboratory as described previously.[39] The MnO standard consisted of MnO nanoparticles synthesized using the inert gas condensation technique, which have a

similar spectrum to sputtered MnO in literature.[38, 40] Average oxidation states were determined from linear combinations of standards, minimizing the mean square error.

III. Results and Discussion

We explore three different types of catalysts in this study. The first is MnO deposited on smooth GC (s-GC MnO), similar to our previous study. As seen by SEM, the morphology of this sample is relatively smooth (Fig. 1a) with a textured surface (inset). Some of these s-GC MnO samples were annealed to Mn_2O_3 (Fig. 1b). The annealing causes a loss of conformality as the underlying GC substrate reacts under the high temperatures and the MnO_x is now seen as the brighter spots in image. These samples have previously been characterized by electrochemistry, and the results suggested that the annealed sample had a higher surface area that benefitted the electrochemical activity.[36] To create an even higher surface area catalyst, the ability to deposit conformal thin films by ALD was leveraged. The partial coverage of MnO_x on the annealed GC was removed, creating a HSA-GC, as seen in Fig. S1. Another ALD MnO deposition was then performed on HSA-GC substrate (Fig. S1), allowing for conformal MnO_x coating of a substrate with approximately the same surface area as the annealed samples (HSA-GC MnO_x, Fig. 1c). The samples shown in Fig. 1(a-c) all began with 40 +/- 2 nm of ALD-MnO_x.

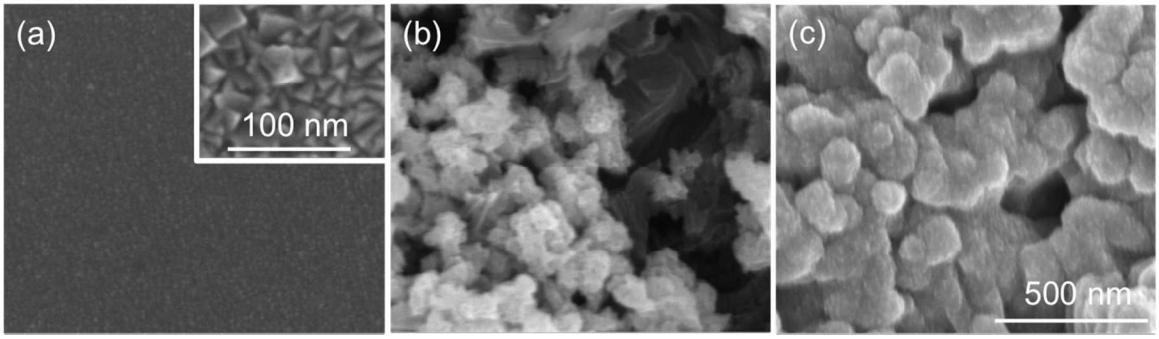

Figure 1: SEM micrographs of (a) s-GC MnO_x, (b) annealed MnO_x, and (c) HSA-GC MnO_x samples. The as-deposited ALD MnO_x has a textured surface as shown in the inset. All samples began with 40 nm MnO_x.. The annealing process results in a porous GC substrate. SEM images (except inset) are scaled to 500 nm scale bar.

The activity of the s-GC MnO_x, HSA-MnO_x, and annealed MnO_x for OER in 0.1 M KOH was tested using cyclic voltammetry. The voltage was swept from 0.05 to 1.8 V_{RHE} in 0.1 M KOH. Consistently, the MnO_x samples deposited on HSA-GC showed the best activity followed by the annealed sample, and lastly the sample on s-GC, as measured by the overpotential needed to achieve a current density of 5 mA cm^{-2}. These trends are illustrated in Fig. 2a, which plots the fifth OER sweep for samples beginning with 40 nm of MnO. The slightly higher activity of the annealed sample compared to the s-GC sample in this thickness range is in agreement with our previous study on MnO_x. The HSA-GC MnO_x shows one of the best activities amongst thin films of MnO_x OER catalysts (see SI).

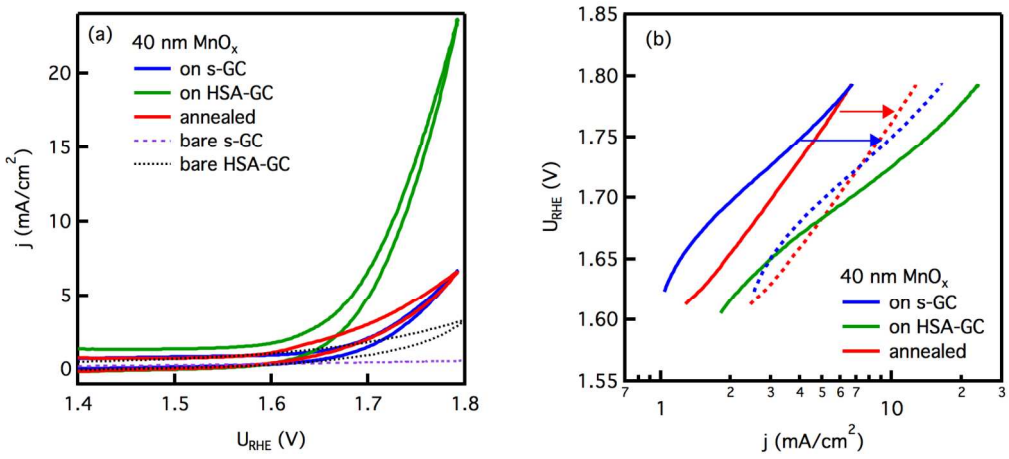

Figure 2: MnO_x/GC catalysts were tested for their activity for the OER using CV. The fifth sweep is displayed in (a). The MnO_x deposited on the HSA-GC shows the highest activity, followed by the annealed catalyst and then the s-GC MnO_x. The substrates are shown as dashed lines for reference. (b) Normalizing the current by surface area to the HSA-GC MnO_x sample using the capacitance ratio reveals that the materials all display similar normalized activity, suggesting that surface area may account for the main differences in catalytic activity for OER. The solid lines are normalized by the geometric surface area and the dashed lines are normalized by the surface area of the MnO_x.

We hypothesize that the surface area of the MnO_x may be the main determinant in catalytic activity of these samples. Although calculating the exact surface area is difficult for oxide materials, we can estimate the ratio of the surface areas between different samples by comparing the current density in a region of the CV where no reaction is occurring (the capacitive current). The capacitive current scales with surface area, and, assuming two surfaces with similar properties, can be used to give an approximate ratio of surface areas. Table 2 lists the measured ratios of 40 nm samples of the HSA-GC MnO_x to s-GC MnO_x and annealed MnO_x to s-MnO_x at 1.26 V, a potential where the capacitive current dominates. Since the catalyst may change during cycling due to phase changes and corrosion, we have tabulated these values at different points during the repetitive cycling. The capacitive measurements show that we successfully created a much higher number of active sites in the HSA-GC MnO_x than the s-GC MnO_x through

the use of a nano-structured substrate. The ratio between the capacitive current of the HSA-GC MnO_x and the s-GC MnO_x is 2.2 initially and 3.2 after 11 cycles. This is in good agreement with the increased roughness of the substrate, which has an estimated increase in surface area ranging from 2-5 (HSA GC/s-GC) based on capacitance measurements. Similarly, the capacitive current ratio of the HSA-GC MnO_x to the annealed MnO_x is initially 1.3 and increases to 1.5 after 11 cycles. The capacitance of MnO_x is higher than the capacitance of glassy carbon, so although the annealed sample also has a high surface area, its capacitance is lower since it is only partly covered with MnO_x.[41] Overall, these measurements show that the HSA-GC MnO_x sample has significantly more electrochemically exposed MnO_x sites than both the annealed and s-GC MnO_x and this difference increases with cycling. Other samples at different thicknesses display similar trends of enhanced surface area for the HSA samples, a difference that increases with cycling. We emphasize that this method provides only an estimate of the different surface areas. An estimate of the surface area ratio found by the area under the redox feature at 0.96 V_{RHE} along with surface area estimates found from capacitance ratios at different voltages show similar trends and are within 30% of the values reported in Table 2 (see SI).

Table 2: Comparison of MnO_x surface areas.

Current ratio at 1.26 V_{RHE}	1st OER cycle	5th OER cycle	11th OER cycle
HSA-GC MnO_x/s-GC MnO_x	2.2	2.5	3.4
Annealed MnO_x/s-GC MnO_x	1.3	1.3	1.5

To investigate the effect of surface area on catalytic activity, we construct Tafel plots, in which electrochemical activity is normalized by the estimate of the relative electrochemical surface areas of the samples (**Fig 2b**). In this plot, we assume a surface area of 1 for the HSA-GC MnO_x and scale the areas of the other samples by the calculated ratios of capacitance from Table 2, using the capacitance in the 5th OER cycle. In the figure, the solid lines are the measured current densities normalized to the geometric surface area and the dashed lines are the HSA-normalized current densities. The significant shift of the dashed lines toward the curve of the HSA-GC MnO_x catalyst indicates that the catalysts' activities are similar to one another when scaled by MnO_x surface area and suggests that the surface area alone could account for the measured differences in activity.

Although ALD can be used to deposit conformal and active films over nanostructured surfaces, the changing capacitive currents with cycling suggest that the surface area of the ALD MnO_x catalysts is modified upon exposure to oxidative potentials. **Fig. 3** shows redox features likely corresponding to Mn^{2+} to Mn^{3+} and Mn^{3+} to Mn^{4+}.[42] The dashed lines are representative of the initial characterization in N_2 saturated electrolyte performed to observe these redox features. The solid lines correspond to the 5th OER sweep in N_2 saturated electrolyte. After cycling, the feature at ~0.65 V_{RHE} corresponding to Mn^{2+} to Mn^{3+} decreases for the as-deposited ALD MnO samples on both the HSA-GC and s-GC. On the other hand, the Mn^{3+} to Mn^{4+} feature at ~0.96 V_{RHE} increases upon cycling. The shift in the peak position and change in the size of the redox

curves in Fig. 3 suggest that the as-deposited catalyst is becoming both oxidized and roughened with exposure to the OER conditions. In the annealed sample, the Mn^{2+} to Mn^{3+} feature is not present initially, reflecting its already more oxidized state. This sample's Mn^{3+} to Mn^{4+} feature also increases with cycling, suggesting changes in the annealed sample as well.

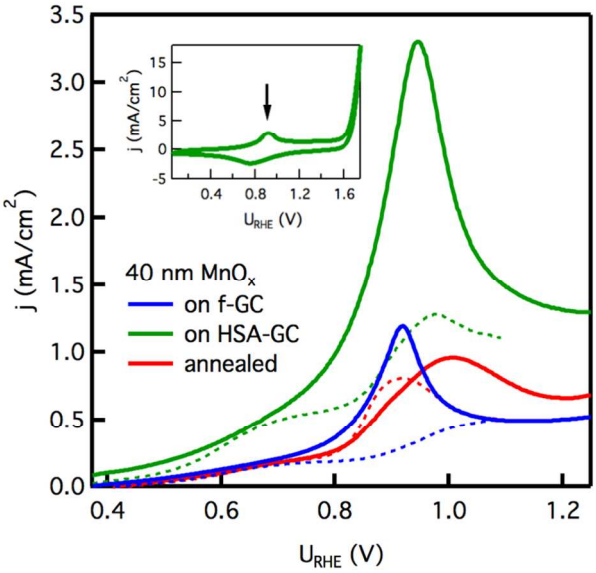

Figure 3: Redox features corresponding to the Mn electrochemical oxidation before (dashed) and after (solid) OER exposure. The location of the features in a standard CV are shown in the inset. The oxidation feature at ~0.65 V likely corresponding to Mn^{2+} to Mn^{3+} disappears with exposure to OER conditions and the feature at ~0.96 V corresponding to Mn^{3+} to Mn^{4+} grows with exposure to OER. This likely reflects the increased surface area and oxidation under OER conditions.

To further investigate the impact of cycling on oxidation state, the samples were characterized using XAS and SEM. We had previously shown by X-ray photoelectron spectroscopy (XPS) and X-ray diffraction (XRD) that the s-GC MnO_x and the annealed sample begin at different oxidation states, with the as-deposited s-GC MnO_x consisting of MnO with a slightly oxidized surface, and the annealed sample containing Mn_2O_3.[36] We hypothesized that the samples oxidized to similar oxidation states under OER conditions, but XPS did not have the sensitivity required to adequately characterize

these changes. Mn L-edge XAS is a more powerful technique, probing the (dipole) transitions from the Mn2p level to the unoccupied 3d valence states.[43] Transition metal L-edge XAS is a rich spectroscopy that is sensitive to oxidation state, spin, symmetry, and charge transfer.[44] As shown in Fig 4a, Mn L-edge XAS, displays distinct differences for various Mn oxide standards, overcoming some of the difficulties associated with assignment of oxidation from XPS alone.[45]

We use Mn L-edge XAS to understand the changes in oxidation state of the catalysts under OER conditions. Both the AEY and TEY signals were collected allowing roughly the top 2 nm and top 4 nm of the surface to be probed, respectively. The AEY signal provides greater surface sensitivity than the TEY signal due to the short escape depth of the Auger electrons. In Figs. 4b and 4c, the TEY signal is drawn as a solid colored line and the AEY signal is drawn as a solid grey line. The average oxidation state of the samples was determined by fitting the normalized TEY spectra with linear combinations of the reference MnO_x standards seen in Fig. 4a, and the average oxidation states for the TEY are summarized in Table 2. A sample fitting is shown in the SI.

First, we establish the initial properties of the as prepared ALD-MnO and annealed MnO_x using Mn L-edge spectroscopy (Fig. 4b). Inspection of the as-deposited ALD MnO_x (blue line) demonstrates that the film consists of MnO with a slightly oxidized surface, consistent with previous XPS results.[36] The measurement shown is for a s-GC MnO_x sample, but is representative of both HSA-GC and s-GC MnO_x catalysts. The difference between the AEY and TEY signals indicates that for the ALD MnO_x, the

surface oxidation is graded with greater oxidation near the surface, and that the oxidation decreases over 2-4 nm. The average oxidation state of the Mn in the first 4 nm is 2.7. The annealed sample (red line), on the other hand, is mostly Mn^{3+}, closely matching Mn_2O_3 standard and has an average oxidation state of 3.0. The AEY and TEY signals are similar to one another, consistent with the bulk change in the oxidation due to the annealing process seen earlier by XRD.[36]

We hypothesize that these oxidation states will change under OER conditions. To investigate the effect of OER potentials on oxidation state, we hold each catalyst at an OER relevant potential (1.65 V_{RHE}) for 30 minutes and then promptly remove the sample from the electrolyte for further characterization using Mn L-edge XAS. The extent of phase transformation evaluated using Mn L-edge XAS is shown in Fig. 4c. It is immediately apparent that both the as-deposited and the annealed MnO_x samples oxidize upon exposure to OER potentials. For the probe depths considered, the as-deposited MnO sample experienced the greatest change in oxidation, going from an average Mn oxidation of 2.7 to an average Mn oxidation state of 3.6. Interestingly, after OER testing, the TEY (blue) and AEY (grey) signals of the as-deposited MnO sample are similar (Fig. 4c). This shows that the depth of this oxidation occurs beyond the surface region, although there is a very slight increase in the shoulder at 643 eV for the AEY signal, indicative of a greater MnO_2 contribution on the surface of the film. The annealed sample, on the other hand, also oxidizes, but only from 3.0 to 3.2 (Fig. 4c). Surprisingly, this means that after OER conditioning, the annealed sample is now less oxidized in the first 2-4 nm compared to the tested ALD MnO sample. In addition, the AEY is slightly

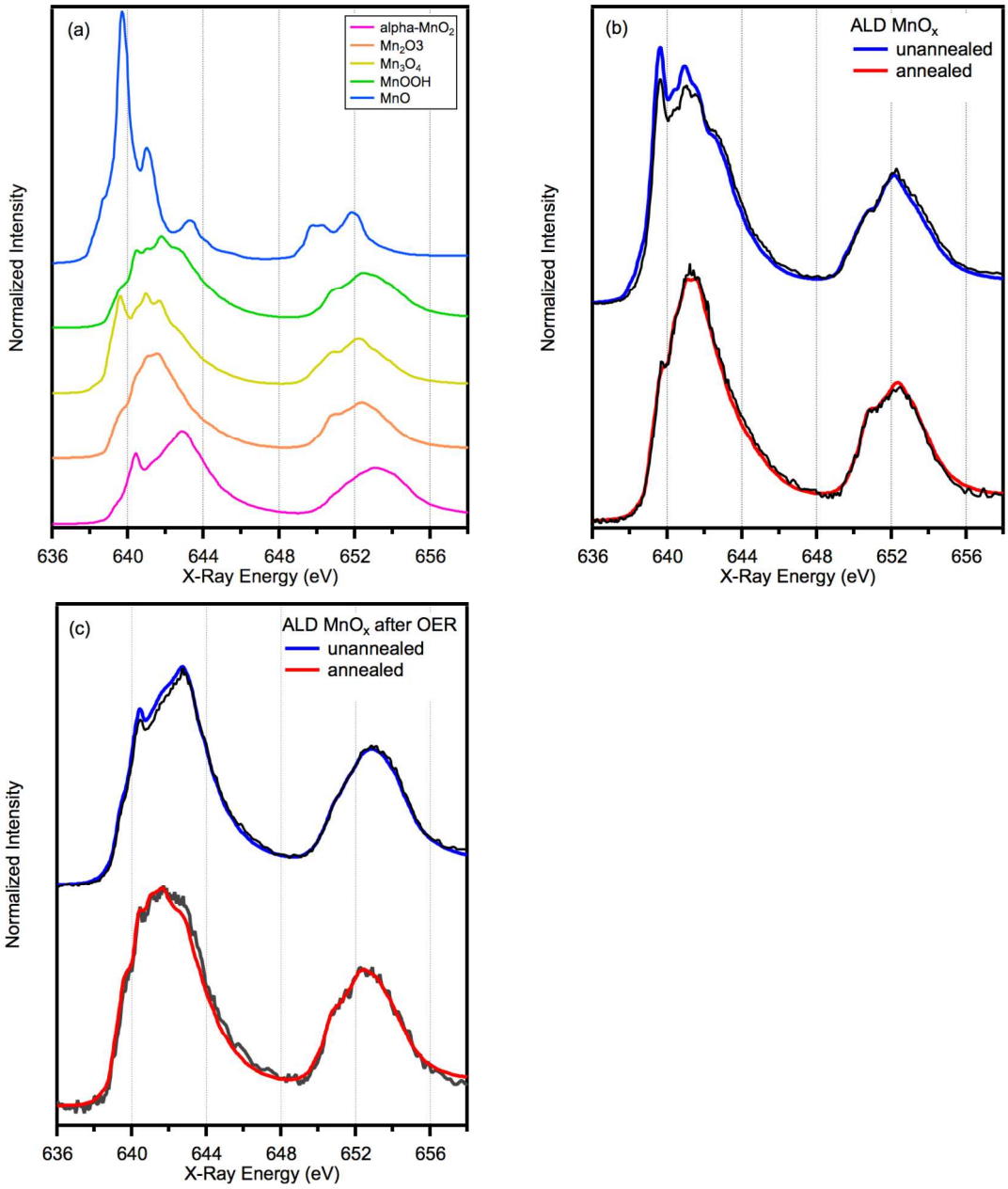

Figure 4: XAS of the Mn-L edge gives information on the oxidation state of the MnO_x thin film. (a) The TEY of different manganese oxides used as standards for calculating the average oxidation state. (b) TEY of the Mn-L edge for the as-deposited MnO that is representative of both the HSA-GC and s-GC (blue) and the annealed MnO_x (red). The AEY signal is plotted in grey. The initial thickness of these samples was ~32 nm. (c) The Mn-L edge spectra for as-deposited MnO_x and annealed MnO_x after 30 minutes of OER exposure. The samples have oxidized during testing. Differences in the AEY and TEY signal indicate differences in the extent of the oxidation of the surface and bulk.

different from the TEY, with an additional feature at 643 eV. Based on the peak position, we speculate that this corresponds to a layer of MnO_2 on the surface, but that the oxidation is unable to penetrate deeply into the film over the time period tested. Previous reports have hypothesized that heat treatments can hinder the ability of electrodeposited MnO_x to change oxidation states in films.[39] Our results suggests that this is also true ALD-deposited MnO.

Table 3: Average Mn oxidation state from TEY Mn L-edge XAS measurements

	Initial	After OER
As-deposited	2.7	3.6
Annealed	3.0	3.2

The changing oxidation states under OER conditions also has an impact on the film morphology and surface area. SEM imaging of the catalysts after OER testing indicates that large changes are occurring in the s-GC MnO_x and HSA-GC MnO_x samples (**Fig. 5a-b**). In both samples, the MnO_x loses its conformality and platelets form. This is consistent with a large phase transformation. The formation of platelets changes the distance charge must travel to the electrode, likely reducing it in localized areas, but it also leads to a local reduction in the amount of MnO_x protecting the electrode from the surface. In addition, the formation of the platelets may partially account for the increase in the surface area under OER conditions. The annealed sample, in contrast, remains relatively unchanged as viewed by SEM (**Fig. 5c**), consistent with the smaller changes in oxidation as shown by the XAS measurements. The annealed sample began with only a partial coating, so both glassy carbon and MnO_x remain exposed.

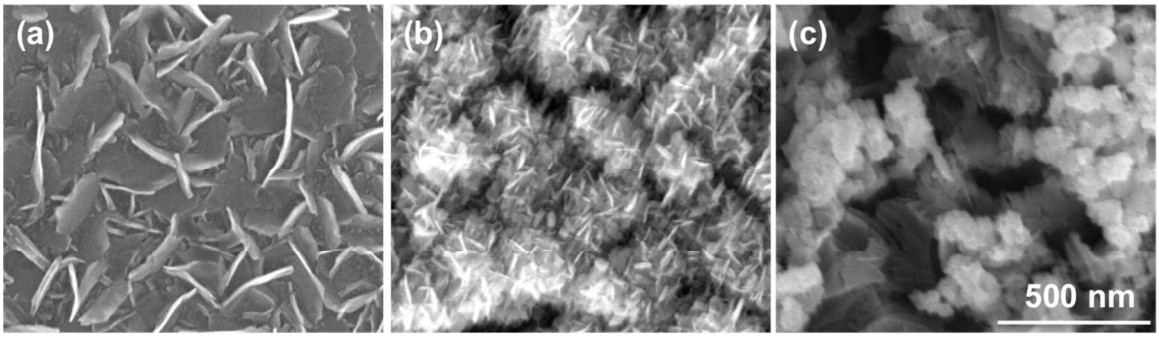

Figure 5: SEM images reveal changes in the morphology of the catalyst after OER testing. Platelets form in the s-GC MnO_x (a) and HSA-GC MnO_x (b) catalysts. Visible changes are not seen in the annealed sample (c).

From these results, it is evident that the preparation route can impact the depth of the oxidation and the changes in the morphology of the MnO_x under OER conditions. Despite these differences, we suggest that both the as-deposited and annealed samples will have similar active sites and that the depth of oxidation is accountable for the differences in the XAS signal. It has been calculated that a O* covered MnO_2 surface is the thermodynamically stable state under OER conditions[46] and the XAS fittings of both the annealed and the as-deposited samples after OER contain MnO_2 components. While it is possible that kinetics may restrict the ability of both samples to oxidize to identical active states, under the electrochemical testing conditions, the activity of the materials appears very similar. It appears that under alkaline conditions, many initial oxidation states may oxidize to active OER states and that the MnO_x surface area can play a dominant role in the activity of MnO_x for OER.[39, 47]

Given the roughening and oxidation that occur naturally under OER conditions for the as-deposited samples, it is reasonable to consider whether the nanostructured template is necessary for the high geometric activity. The HSA-GC MnO has a larger volume of MnO_x present compared to the s-GC MnO sample of the same thickness. It is

possible that if the same volume of MnO_x that is present in the HSA-GC MnO_x samples were deposited as a thicker film on a s-GC, the s-GC sample could, when restructured under OER conditions, achieve a similarly high density of active sites. In addition, the electrochemically accessible area is often not simply the surface of the MnO_x, but contained at sites within the film.[48-50] Some of the most active MnO_x electrocatalysts consist of MnO_x on the order of millimeters thick.[51] Therefore, in the next part of the study, we look at whether a nanostructured substrate is necessary to achieve the high activity on geometric surface area basis. To test the effect of the nano-structured substrate, we sought to deposit MnO on a s-GC substrate such that it would have approximately the same volume of MnO as on a HSA substrate. We compare the OER activity of 15 nm of MnO on a HSA substrate with that of both 40 and 92 nm of MnO on a flat substrate. Assuming a roughness with effective surface area 2-5 times larger than the HSA-GC (consistent with capacitance measurements), the 15 nm HSA-GC sample would have the volumetric equivalent of between 30-75 nm MnO on s-GC. Samples were first cycled 0.05 V_{RHE} and 1.1 V_{RHE} as with the previous samples, followed by OER testing. As can be seen in **Fig. 6**, the geometric activities of both the 40 and 92 nm s-GC samples are much lower than the 15 nm MnO on HSA-GC, and hence the activity does not scale with MnO volume. Limitations in charge and mass transport likely lead to significantly lower OER activity for the thicker films. The deleterious effects of thickness observed in this study, seen even at 92 nm, occur at lower thicknesses than those reported for other MnO_x systems, possibly related to a compact thin film deposited by ALD that impedes electrolyte intercalation.[49, 51] A nano-structured substrate such as that of HSA-GC, therefore, allows for the dispersion of the same volume of MnO_x at a

much smaller thickness, providing for a shorter distance for mass and charge transport and thus enhanced OER activity. Consequently, ALD provides a route to evenly coat nano-structured substrates to produce active electrocatalysts. The surface area of these catalysts can then be roughened by electrochemical testing.

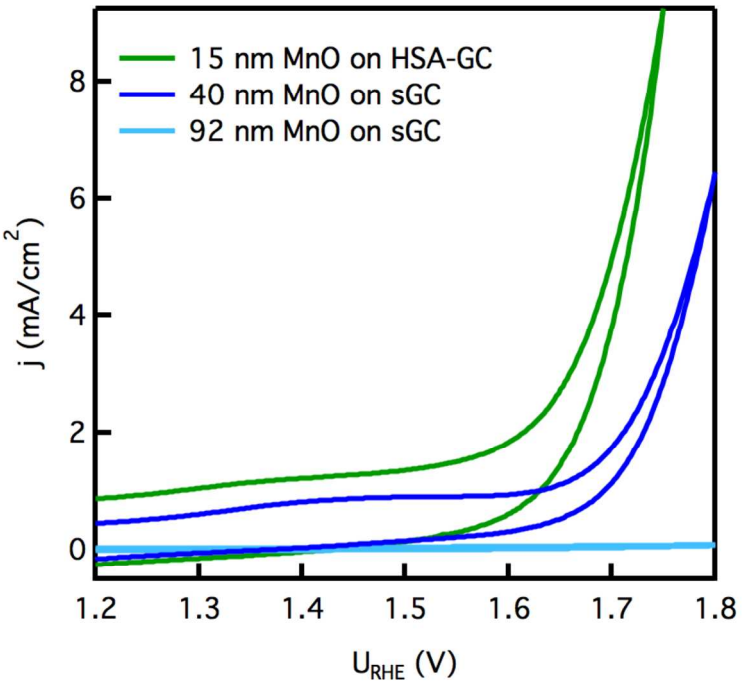

Figure 6: The nanostructured substrate is necessary to achieve the high geometric activity. The 15 nm sample on the HSA-GC has the volumetric equivalent to approximately 30-75 nm of MnO on s-GC, but is distributed thinly so mass transport and charge transport are not limiting.

We conclude with some thoughts about the application of ALD MnO based on the results from this work. Toward catalyst design, the ALD MnO shows many promising possibilities. Under anodic conditions in basic solutions, it restructures to a higher oxide that is active for the OER, without a need for molecular oxidants that were shown to be important in neutral solutions.[52] The ALD process also allows for the deposition on a

high surface area, nanostructured substrate, which can further enhance catalytic activity on a geometric basis. ALD has previously been used to coat high surface templates such as inverse opal structures with catalysts with great success.[53, 54] Moreover, there does not appear to be a need to anneal the catalyst in order to achieve higher activity, which allows for coating on temperature-sensitive substrates (100 - 300 °C ALD window compared to a 480 °C anneal). On the other hand, since we are depositing compact dense films by ALD, charge transport may become limiting at smaller film thicknesses than by other methods.

Applications of ALD MnO to PEC photoanodes as both a passivating layer and an electrocatalyst in basic solutions is less encouraging, even though the ALD technique has shown much promise in passivating semiconducting electrodes because of its ability to create dense, pin-hole free layers.[11, 12, 34] This work shows that ALD MnO is unable to maintain its high quality film properties with exposure of its surface to the OER conditions. In a previous report that attempted to stabilize Si with ALD-MnO to produce a photoanode, the catalyst remained stable for only 10 – 30 minutes.[35] As suggested in Ref 35 and as we herein clearly show, depositing MnO catalysts and holding at OER potentials can produce a phase change that results in the loss of the conformal film coating. As a result, for metal oxide passivating layers in PEC devices, deposition of the catalyst in the oxidation state that will be thermodynamically favored under the OER conditions is important to creating a stable protective layer. Such an approach could minimize phase changes and lead to high film quality throughout the operation of the

device. For MnO_x films, better strategies may therefore be to deposit Mn_2O_3 or MnO_2 by ALD, or to add an additional stabilizing layer.

IV. Conclusions

In this work, we explore methods to enhance the activity of ALD-MnO for OER in 0.1 M KOH. We show that both ALD-MnO and Mn_2O_3 oxidize under OER conditions. Although the oxidation states of these films are different when averaged over the first 2-4 nm, the activity appears to be primarily related to MnO_x surface area. In agreement with several recent studies, multiple initial oxidation states may be active for OER in basic conditions, although as shown in this study, the oxidation state impacts the degree of restructuring.[25, 47, 55] Using the ability of ALD to deposit on nanostructured substrates, higher geometric activity was achieved. The nanostructured substrate is necessary to allow for sufficient dispersion of the catalyst and a reduction in the distance charge must travel through the electrode. Reconstruction of the MnO_x under OER conditions may be beneficial for the catalytic activity, but is detrimental if using the MnO_x as a passivating layer. These studies may be used to guide further catalyst development.

V. Acknowledgments

This work was supported as part of the Center on Nanostructuring for Efficient Energy Conversion (CNEEC), an Energy Frontier Research Center funded by the U.S. Department of Energy, Office of Science, Basic Energy Sciences under Award # DE-SC0001060. K.L.P. acknowledges a graduate fellowship through the NSF.

VI. References

1. Detavernier, C.; Dendooven, J.; Pulinthanathu Sree, S.; Ludwig, K. F.; Martens, J. A. *Chemical Society Reviews* **2011,** 40, (11), 5242-5253.
2. Peng, Q.; Lewis, J. S.; Hoertz, P. G.; Glass, J. T.; Parsons, G. N. *J Vac Sci Technol A* **2012,** 30, (1), 010803.
3. Yang, X.; Du, C.; Liu, R.; Xie, J.; Wang, D. *J Catal* **2013,** 304, (0), 86-91.
4. Liu, C.; Dasgupta, N. P.; Yang, P. *Chem Mater* **2013,** 26, (1), 415-422.
5. Jiang, X.; Huang, H.; Prinz, F. B.; Bent, S. F. *Chem Mater* **2008,** 20, (12), 3897-3905.
6. George, S. M. *Chem Rev* **2010,** 110, (1), 111-131.
7. Kim, H.; Lee, H.-B.-R.; Maeng, W. J. *Thin Solid Films* **2009,** 517, (8), 2563-2580.
8. Marichy, C.; Bechelany, M.; Pinna, N. *Advanced Materials* **2012,** 24, (8), 1017-1032.
9. Lewis, N. S.; Nocera, D. G. *P Natl Acad Sci USA* **2007,** 104, (50), 20142-20142.
10. Pinaud, B. A.; Benck, J. D.; Seitz, L. C.; Forman, A. J.; Chen, Z.; Deutsch, T. G.; James, B. D.; Baum, K. N.; Baum, G. N.; Ardo, S.; Wang, H.; Miller, E.; Jaramillo, T. F. *Energ Environ Sci* **2013,** 6, (7), 1983-2002.
11. Hu, S.; Shaner, M. R.; Beardslee, J. A.; Lichterman, M.; Brunschwig, B. S.; Lewis, N. S. *Science* **2014,** 344, (6187), 1005-1009.
12. Chen, Y. W.; Prange, J. D.; Duhnen, S.; Park, Y.; Gunji, M.; Chidsey, C. E. D.; McIntyre, P. C. *Nat Mater* **2011,** 10, (7), 539-544.
13. Lu, J.; Elam, J. W.; Stair, P. C. *Accounts of Chemical Research* **2013,** 46, (8), 1806-1815.
14. Dasgupta, N. P.; Liu, C.; Andrews, S.; Prinz, F. B.; Yang, P. *J Am Chem Soc* **2013,** 135, (35), 12932-12935.
15. Gür, T. M.; Bent, S. F.; Prinz, F. B. *The Journal of Physical Chemistry C* **2014,** 118, (37), 21301-21315.
16. Walter, M. G.; Warren, E. L.; McKone, J. R.; Boettcher, S. W.; Mi, Q. X.; Santori, E. A.; Lewis, N. S. *Chem Rev* **2010,** 110, (11), 6446-6473.
17. Man, I. C.; Su, H. Y.; Calle-Vallejo, F.; Hansen, H. A.; Martinez, J. I.; Inoglu, N. G.; Kitchin, J.; Jaramillo, T. F.; Norskov, J. K.; Rossmeisl, J. *Chemcatchem* **2011,** 3, (7), 1159-1165.
18. Doyle, R. L.; Godwin, I. J.; Brandon, M. P.; Lyons, M. E. G. *Physical Chemistry Chemical Physics* **2013,** 15, (33), 13737-13783.
19. McCrory, C. C. L.; Jung, S.; Peters, J. C.; Jaramillo, T. F. *J Am Chem Soc* **2013,** 135, (45), 16977-16987.
20. Jiao, F.; Frei, H. *Chem Commun* **2010,** 46, (17), 2920-2922.
21. Zaharieva, I.; Chernev, P.; Risch, M.; Klingan, K.; Kohlhoff, M.; Fischer, A.; Dau, H. *Energ Environ Sci* **2012,** 5, (5), 7081-7089.
22. Mohammad, A. M.; Awad, M. I.; El-Deab, M. S.; Okajima, T.; Ohsaka, T. *Electrochim Acta* **2008,** 53, (13), 4351-4358.
23. Gorlin, Y.; Jaramillo, T. F. *J Am Chem Soc* **2010,** 132, (39), 13612-13614.
24. Kanady, J. S.; Tsui, E. Y.; Day, M. W.; Agapie, T. *Science* **2011,** 333, (6043), 733-736.

25. Huynh, M.; Bediako, D. K.; Nocera, D. G. *J Am Chem Soc* **2014,** 136, (16), 6002-6010.
26. Nørskov, J. K.; Bligaard, T.; Logadottir, A.; Bahn, S.; Hansen, L. B.; Bollinger, M.; Bengaard, H.; Hammer, B.; Sljivancanin, Z.; Mavrikakis, M.; Xu, Y.; Dahl, S.; Jacobsen, C. J. H. *J Catal* **2002,** 209, (2), 275-278.
27. Zorn, K.; Giorgio, S.; Halwax, E.; Henry, C. R.; Grönbeck, H.; Rupprechter, G. *J Phys Chem C* **2011,** 115, (4), 1103-1111.
28. Muñiz, K. *Angewandte Chemie - International Edition* **2009,** 48, (50), 9412-9423.
29. King, J. S.; Wittstock, A.; Biener, J.; Kucheyev, S. O.; Wang, Y. M.; Baumann, T. F.; Giri, S. K.; Hamza, A. V.; Baeumer, M.; Bent, S. F. *Nano Letters* **2008,** 8, (8), 2405-2409.
30. Viswanathan, V.; Pickrahn, K.; Luntz, A. C.; Bent, S. F.; Norskov, J. K. *Nano Letters* **2014**.
31. Liu, R.; Zheng, Z.; Spurgeon, J.; Brunschwig, B. S.; Yang, X. *Energ Environ Sci* **2014**.
32. Pierret, R. F., *Semiconductor Device Fundamentals*. Pearson Education: 1996.
33. Seitz, L. C.; Chen, Z.; Forman, A. J.; Pinaud, B. A.; Benck, J. D.; Jaramillo, T. F. *ChemSusChem* **2014,** 7, (5), 1372-1385.
34. Paracchino, A.; Mathews, N.; Hisatomi, T.; Stefik, M.; Tilley, S. D.; Gratzel, M. *Energ Environ Sci* **2012,** 5, (9), 8673-8681.
35. Strandwitz, N. C.; Comstock, D. J.; Grimm, R. L.; Nichols-Nielander, A. C.; Elam, J.; Lewis, N. S. *The Journal of Physical Chemistry C* **2013,** 117, (10), 4931-4936.
36. Pickrahn, K. L.; Park, S. W.; Gorlin, Y.; Lee, H. B. R.; Jaramillo, T. F.; Bent, S. F. *Adv Energy Mater* **2012,** 2, (10), 1269-1277.
37. Burton, B. B.; Fabreguette, F. H.; George, S. M. *Thin Solid Films* **2009,** 517, (19), 5658-5665.
38. Gorlin, Y.; Chung, C.-J.; Nordlund, D.; Clemens, B. M.; Jaramillo, T. F. *ACS Catalysis* **2012,** 2, (12), 2687-2694.
39. Gorlin, Y.; Nordlund, D.; Jaramillo, T. F. *ECS Transactions* **2013,** 58, (1), 735-750.
40. Gilbert, B.; Frazer, B. H.; Belz, A.; Conrad, P. G.; Nealson, K. H.; Haskel, D.; Lang, J. C.; Srajer, G.; De Stasio, G. *The Journal of Physical Chemistry A* **2003,** 107, (16), 2839-2847.
41. This method likely slightly overestimates the amount of MnOx on the annealed sample since the exposed glassy carbon will contribute to the capacitive current, but should give an approximate amount. The discrepancy may explain the slightly lower activity of the annealed sample discussed below.
42. Lima, F. H. B.; Calegaro, M. L.; Ticianelli, E. A. *Electrochim Acta* **2007,** 52, (11), 3732-3738.
43. Qiao, R.; Chin, T.; Harris, S. J.; Yan, S.; Yang, W. *Current Applied Physics* **2013,** 13, (3), 544-548.
44. Groot, F. d.; Kotani, A., *Core Level Spectroscopy of Solids*. Taylor & Francis Ltd: Hoboken, New Jersey, USA, 2008.
45. Gorlin, Y.; Jaramillo, T. F. *J Electrochem Soc* **2012,** 159, (10), H782-H786.

46. Su, H.-Y.; Gorlin, Y.; Man, I. C.; Calle-Vallejo, F.; Norskov, J. K.; Jaramillo, T. F.; Rossmeisl, J. *Physical Chemistry Chemical Physics* **2012,** 14, (40), 14010-14022.
47. Singh, A.; Hocking, R. K.; Chang, S. L. Y.; George, B. M.; Fehr, M.; Lips, K.; Schnegg, A.; Spiccia, L. *Chem Mater* **2013,** 25, (7), 1098-1108.
48. Trasatti, S. *Electrochim Acta* **1991,** 36, (2), 225-241.
49. Gorlin, Y.; Lassalle-Kaiser, B.; Benck, J. D.; Gul, S.; Webb, S. M.; Yachandra, V. K.; Yano, J.; Jaramillo, T. F. *J Am Chem Soc* **2013,** 135, (23), 8525-8534.
50. Bergmann, A.; Zaharieva, I.; Dau, H.; Strasser, P. *Energ Environ Sci* **2013,** 6, (9), 2745-2755.
51. Morita, M.; Iwakura, C.; Tamura, H. *Electrochim Acta* **1978,** 23, (4), 331-335.
52. Indra, A.; Menezes, P. W.; Zaharieva, I.; Baktash, E.; Pfrommer, J.; Schwarze, M.; Dau, H.; Driess, M. *Angew Chem Int Edit* **2013,** 52, (50), 13206-13210.
53. Williams, V. O.; DeMarco, E. J.; Katz, M. J.; Libera, J. A.; Riha, S. C.; Kim, D. W.; Avila, J. R.; Martinson, A. B. F.; Elam, J. W.; Pellin, M. J.; Farha, O. K.; Hupp, J. T. *ACS Applied Materials & Interfaces* **2014,** 6, (15), 12290-12294.
54. Riha, S. C.; Klahr, B. M.; Tyo, E. C.; Seifert, S.; Vajda, S.; Pellin, M. J.; Hamann, T. W.; Martinson, A. B. F. *Acs Nano* **2013,** 7, (3), 2396-2405.
55. Robinson, D. M.; Go, Y. B.; Mui, M.; Gardner, G.; Zhang, Z.; Mastrogiovanni, D.; Garfunkel, E.; Li, J.; Greenblatt, M.; Dismukes, G. C. *J Am Chem Soc* **2013,** 135, (9), 3494-3501.